

UNSUPERVISED DETECTION OF PLANETARY CRATERS BY A MARKED POINT PROCESS

G. Troglio^{1,2}, J. A. Benediktsson¹, J. Le Moigne³, G. Moser², S. B. Serpico²

¹ University of Iceland, Faculty of Electrical and Computer Engineering,

Reykjavik, Iceland

² University of Genoa, Dept. of Biophysical and Electronic Engineering,

Genoa, Italy, e-mail: giulia.troglio@unige.it

³ NASA Goddard Space Flight Center, Software Engineering Division,

Code 580, Greenbelt, MD, USA,

ABSTRACT

With the launch of several planetary missions in the last decade, a large amount of planetary images is being acquired. Preferably, automatic and robust processing techniques need to be used for data analysis because of the huge amount of the acquired data. Here, the aim is to achieve a robust and general methodology for crater detection. A novel technique based on a marked point process is proposed. First, the contours in the image are extracted. The object boundaries are modeled as a configuration of an unknown number of random ellipses, i.e., the contour image is considered as

a realization of a marked point process. Then, an energy function is defined, containing both an a priori energy and a likelihood term. The global minimum of this function is estimated by using reversible jump Monte-Carlo Markov chain dynamics and a simulated annealing scheme. The main idea behind marked point processes is to model objects within a stochastic framework: Marked point processes represent a very promising current approach in the stochastic image modeling and provide a powerful and methodologically rigorous framework to efficiently map and detect objects and structures in an image with an excellent robustness to noise.

The proposed method for crater detection has several feasible applications. One such application area is image registration by matching the extracted features.

Index Terms—Crater Detection, Marked Point Process, Markov Chains, Simulated Annealing.

1. INTRODUCTION

With each new planetary mission, the volume of acquired data significantly increases. Different types of data are being collected at different times, by different sensors, and from different view-points. Feature extraction, i.e., extraction of spatial features in the images, is typically the first step in most image analysis processes. For instance, registration is an essential task to jointly exploit, integrate, or compare all these different data and usually requires a prior accurate extraction of the spatial features in the image.

Identification of spatial features on planetary surfaces can be manually performed by human experts but this process can be very time consuming. Therefore, a reliable automatic approach to detect the position, structure, and dimension of each feature is highly desirable. This is a difficult task for several reasons: Limited data are usually available, the contrast of planetary images is generally low (i.e., it is heavily affected by illumination, surface properties and atmospheric state), and the features that are present in

the images can be barely visible due to atmospheric erosion and they may be based on different structure types of variable sizes. Among the typical features in planet-surface imagery, craters play a primary role. Detection of craters has been widely addressed and different approaches have recently been proposed in the literature, based on the analysis of planetary topography data [1], satellite images in the visible spectrum and the infrared spectrum [2]. Here, we focus on optical image-based approaches for crater detection.

The existing techniques can be divided into two main categories; supervised and unsupervised. Supervised methods require the input of an expert and generally use supervised learning concepts to train the algorithm for feature extraction. These techniques contemplate a learning phase, in which a training set of images containing craters is labeled by human experts. Craters are then detected by applying the previously trained algorithm to new unlabeled sets of images. In [3], a continuously scalable detector, based on a supervised template matching technique, is applied. In [4], different supervised learning approaches, including ensemble methods, support vector machines (SVM), and continuously-scalable template models, were employed to derive crater detectors from ground-truthed images. The SVM approach with normalized image patches provided the best detection and localization performance. In a different approach, Martins *et al.* [5] adopted a supervised boosting algorithm, originally developed by Viola and Jones [6] in the context of face detection, to identify craters on Mars.

Unsupervised methods are fully automatic and generally based on image-analysis techniques. These approaches generally rely on the identification of circular or elliptical arrangements of edges along the crater boundary. A standard approach is based on the use of a Generalized Hough Transform (GHT) [7]. Examples include the works of Cross [8], Cheng *et al.* [9], Honda *et al.* [10], Leroy *et al.* [11], and Michael [12]. Instead, in [13], the identification of impact craters was achieved through the analysis of the probability volume created as a result of a template matching procedure, approximating the craters as objects of round shape. That unsupervised method enables the identification of round spatial features.

Kim and Muller [14] presented a crater detection method based on texture analysis and ellipse fitting. That method was not robust when applied to optical images. Therefore the authors needed to use also DEM data and fuse them with the optical data.

In subsequent work [15], Kim *et al.* proposed a combination of unsupervised and supervised techniques. In particular, edge detection, template matching, and supervised neural network-based schemes for the recognition of false positives were integrated, in order to automatically detect craters on Mars. In [16], Urbach and Stepinski presented a different approach, which combines unsupervised and supervised techniques, for crater detection in panchromatic planetary images. The method in [16] is based on using mathematical morphology for the detection of craters and on supervised techniques to distinguish between objects and false alarms.

Each of the previously published methodologies for automatic crater detection has its advantages and drawbacks. Although the recent approaches show high detection accuracy, the underlying technology is complicated and its robustness to different types of planetary surfaces and to image quality is not totally satisfactory yet.

Here, a novel automatic and unsupervised approach for the extraction of planetary craters, based on a Marked Point Process (MPP) [17], is proposed (see also [18]). An MPP is an abstract random variable whose realizations are configurations of objects, each object being described by a marked point (see Appendix A for more details). In the proposed method, the objects that are searched for are craters and a novel MPP model is defined to determine their statistical distribution in the image. The boundaries of the regions of interest are considered as a realization of an MPP of ellipses. Hence, the optimum configuration of objects has to be estimated. Similar to Markovian modeling, the "Maximum-A-Posteriori" (MAP) can be proved to be equivalent, under MPP assumption, to the minimization of a suitable energy function. An energy function, which takes into account the interactions between the geometric objects and the way they

fit in the image, is minimized by using a Markov chain coupled with a simulated annealing scheme.

The main novelty of this paper is a novel unsupervised method for crater detection, based on the MPP stochastic modeling technique. Moreover, a new formulation of the likelihood energy function is proposed here, being more appropriate for the analyzed data. In comparison with other techniques, e.g., based on template matching, the proposed approach enables the identification of features of different shapes and orientations and it is applicable to different types of data.

The proposed approach is described in Section 2. Experimental results with real data are presented and discussed in Section 3. Finally, conclusions and ideas for future extensions are presented in Section 4.

2. METHODOLOGY

2.1. Overview of the proposed method

Planetary images show the surface of a planet and its structures. The aim of this study is to automatically detect elliptical structures, such as craters, that are present on a considered planetary surface by using image analysis techniques. The extracted features can be used for the registration of multitemporal, multisensor, and stereo-images.

Different types of spatial features are present in the planetary images, but the most evident ones are generally craters, i.e., objects of approximately elliptical shapes with shadows. Their extraction is a difficult task, because planetary images are blurry, quite noisy, present lack of contrast and uneven illumination, and the represented objects are not well defined.

In order to address this problem, an MPP-based approach, aimed at detecting round and elliptical objects, is proposed here. MPPs enable to model the distribution of complex geometrical objects in a scene (see Appendix A for more details) and have been exploited for different applications in image process-

ing. Marked point processes have been successfully applied to address different problems in terrestrial remote sensing, among which road network extraction [19] and building extraction in dense urban areas [20], [21], [22]. Moreover, in forestry applications, marked point processes have been used to reproduce the spatial distribution of the stems [23]. Here, the method is applied to the detection of features in planetary images.

The context is stochastic and the goal is to minimize an energy on the state space of all possible configurations of objects, using a Markov Chain Monte-Carlo (MCMC) algorithm and a Simulated Annealing (SA) scheme. More properly, a novel MPP is introduced to model the structure of the crater edges in the image.

The overall architecture of the proposed approach for crater detection is shown in Figure 1. First, the

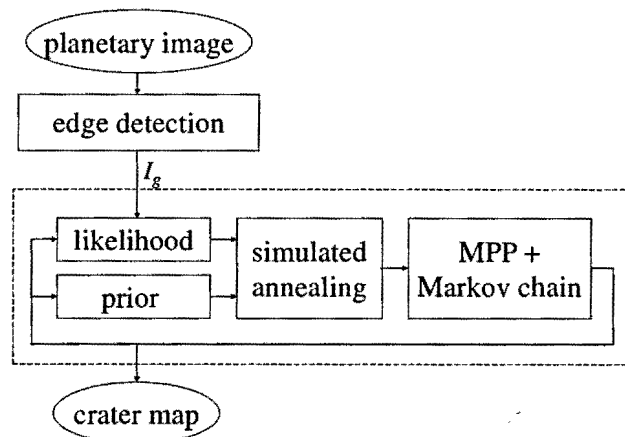


Fig. 1. Flowchart of the proposed approach.

noise is reduced by applying a smoothing filtering operation. Then, in order to produce an edge map I_g , showing the contours of the objects represented in the original image, the Canny edge detector [24] is applied. The Canny detector has been chosen because it guarantees a low error rate, the obtained edge points are well localized, and the width of each detected edge is one pixel.

The result of this first step, I_g , is a binary image that shows the object boundaries. Craters have a

complex structure and, due to their depth and uneven illumination, exhibit shadows. Their borders can be approximated with incomplete non-continuous elliptical curves.

I_g is modeled as a configuration of objects whose positions and attributes are a realization of an MPP X [25]. The MPP X is a process whose realizations are random configurations x of several objects, each belonging to a space $S = P \times K$, where P is the position space, and K the space of the marks, i.e., set of parameters that fully describe each object. Here, the 2D model, used to extract the features of interest, consists of an MPP of ellipses, and each ellipse is represented by a 5-tuple (u, v, a, b, θ) , taking values in the set space

$$S = \overbrace{[0, M] \times [0, N]}^P \times \overbrace{[a_m, a_M] \times [b_m, b_M] \times [0, \pi]}^K, \quad (1)$$

where $(u, v) \in [0, M] \times [0, N]$ are the coordinates of the ellipse center (M and N being the width and height of I_g), a and b are the ellipse axes (ranging in $[a_m, a_M]$ and $[b_m, b_M]$, respectively), and $\theta \in [0, \pi]$ is the ellipse orientation angle.

The probability distribution of this stochastic process is uniformly continuous [26] with respect to a suitable Poisson measure on S (see Appendix A for more details). Operatively, this means that it may be characterized by a density f with respect to this measure. Similarly, the posterior distribution of x conditioned to I_g can also be characterized by a density function f_p with respect to the same measure and a Gibbs formulation is proven to hold for f_p [21]. Hence, one may introduce an energy function U such that

$$f_p(x|I_g) = \frac{1}{Z} \exp\{-U(x|I_g)\} \quad (2)$$

where Z is a normalizing constant. Hence, in order to minimize this posterior distribution, U will be minimized on the space of all configurations x in the feature extraction process.

2.2. The proposed energy function

The energy function takes into account the interactions between the geometric objects x_1, x_2, \dots, x_n in the configuration x (the prior energy U_P), and the way they fit to the data (the likelihood energy U_L)

$$U(x|I_g) = U_P(x) + U_L(I_g|x). \quad (3)$$

The prior term characterizes the general aspect of the desired solution. According to the geometric properties of the configurations of craters, a basic rule is imposed on the prior term of our model. The prior energy, U_P , penalizes overlapping objects in x , which are very unlikely, by adding a repulsion between objects which intersect. The prior energy of our model is

$$U_P(x) = \frac{1}{n} \sum_{x_i \star x_j} R(x_i, x_j) \quad (4)$$

where R is a repulsion coefficient, which penalizes each pair of overlapping objects (denoted as $x_i \star x_j$) in the configuration x . The repulsion coefficient R is calculated as follows

$$R(x_i, x_j) = \frac{x_i \cap x_j}{x_i \cup x_j} \quad (5)$$

where $x_i \cap x_j$ denotes the overlapping area between the two objects x_i and x_j in the configuration ($i, j = 1, 2, \dots, n, i \neq j$) and $x_i \cup x_j$ indicates the sum of the areas covered by the two objects x_i and x_j .

Then, the likelihood term U_L is defined as

$$U_L(I_g|x) = U_S(I_g|x) + U_D(I_g|x), \quad (6)$$

where U_S measures the similarity between the configuration and the data, whereas the data term U_D measures the distance between the objects in the configuration and the contours of the data. Different formulations for the likelihood energy, which have been proposed in previous work on MPP [23,25], have

proven to be unfeasible for planetary data. Hence, a new formulation for U_L , more appropriate for the analyzed data, is proposed here.

In particular, the similarity energy U_S between the data I_g and the current configuration x is defined as a correlation measure¹

$$U_S(I_g|x) = \frac{|\{(u, v) : I_g(u, v) = 1 \ \& \ \Pi(u, v|x) = 1\}|}{|\{(u, v) : I_g(u, v) = 1\}|} \quad (7)$$

where u and v are the spatial coordinates in the image plane; $\Pi(\cdot|x)$ is the projection of the configuration x such that $\Pi(u, v|x) = 1$ if (u, v) belongs to the boundary of at least one ellipse in the configuration x (i.e., if there exists $i \in \{1, 2, \dots, n\}$ such that (u, v) is on the boundary of x_i), and $\Pi(u, v|x) = 0$, otherwise. Consequently, U_S expressed as (7) is equivalent to the definition of a correlation function between the binary images I_g and $\Pi(\cdot|x)$, representing the extracted and the modeled edges, respectively. According to the correlation definition, in the binary case, only nonzero pixels from both images contribute to the value of the correlation. This energy term, which is novel with respect to the MPP literature, resembles analogous correlation measures that have been used for registration purposes [27]. The correlation measure in (7) is considered to be appropriate here because it enables to estimate the match between two binary images (I_g and Π) in a fast and accurate way.

Then, the data energy U_D is calculated at the object level: For each object x_i in the current configuration x a weight parameter W_i , proportional to the distance from the closest detected edge pixel in the data I_g with respect to its dimension, is calculated, i.e.,

$$W_i = \frac{\inf\{\sqrt{(u-u')^2 + (v-v')^2} : I_g(u, v) = 1 \ \& \ \Pi(u', v'|x_i) = 1\}}{\max(a_i, b_i)}, \quad (8)$$

where $\Pi(\cdot|x_i)$ has a meaning similar to above and a_i and b_i are the two ellipse axes associated to the object x_i ($i = 1, 2, \dots, n$).

¹Given a finite set A , we denote by $|A|$ the cardinality (i.e., the number of elements) of A .

The resulting data energy will be

$$U_D(I_g|x) = \frac{1}{n} \sum_{i=1}^n W_i. \quad (9)$$

Then, objects with a low value of W will be favored in the configuration.

2.3. Energy Minimization and Crater Mapping

A Markov Chain Monte-Carlo (MCMC) algorithm [28], coupled with a Simulated Annealing (applied with a given annealing schedule $T(\cdot)$), is used in order to find the configuration x which minimizes U . We stress here that this minimization is carried out with respect to not only the locations and marks of the objects in the MPP realization but also the number of objects, i.e., the proposed method also automatically optimizes the choice of the number of detected craters. In particular, the marked point process X , defined by f , is sampled by using a random jump MCMC algorithm (see Appendix B for more details): It allows to build a Markov chain X_k ($k = 0, 1, \dots$), which jumps between the different dimensions of the space of all possible configurations and, in the ideal case, ergodically converges to the optimum distribution x^* [29]. The final configuration of convergence does not depend on the initial state. The flowchart of the minimization scheme is shown in Figure 2.

At each step, the transition of this chain depends on a set of “proposition kernels”, which are random changes proposed to the current configuration. In order to find the configuration maximizing the density $f_p(\cdot)$ on S , we sample within a Simulated Annealing scheme (SA), which gives us the MAP estimator. SA is an iterative algorithm where at each iteration k a perturbation is proposed to the current configuration at temperature $T(k)$, $k = 1, 2, \dots, K$. This perturbation is accepted or rejected with a probability which ensures that the probability distribution of the Markov chain ergodically converges to $f_p(x)^{\frac{1}{T(k)}}$. Here, the

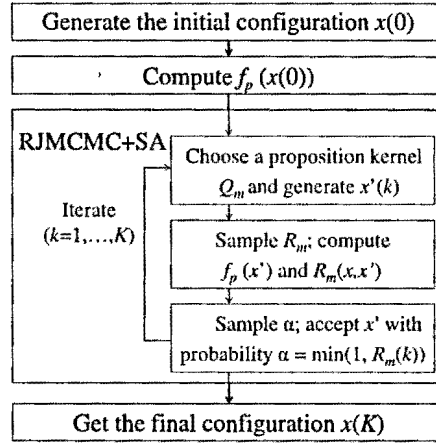


Fig. 2. Flowchart of the proposed minimization scheme.

annealing schedule, $T(\cdot)$, is defined as

$$T(k) = T_I \cdot \left(\frac{T_F}{T_I} \right)^{\frac{k}{K}}, \quad (10)$$

where T_I and T_F are the initial and the final temperatures, respectively, and K is the total number of allowed iterations. In practice, in order to cope with too long computational times, the decrease of the temperature is geometric (as usual in SA for Markov random fields) and does also not imply the ergodic convergence to a probability distribution localized at the minima of $U(x|I_g)$, in contrast, it follows the adaptive approach developed in [30].

The set of proposition kernels are birth and death, translation, dilation, and rotation [31] (see Appendix B for more details). For each proposition kernel m , a Green ratio $R_m(x, x')$ is defined, that tunes the likelihood of replacing configuration x by configuration x' at each SA iteration (analytical details can be found in Appendix B). More precisely, the birth and death kernel consists in proposing, with probability p_B , to uniformly add in S an object to the current configuration x or, with probability $p_D = 1 - p_B$, to remove a randomly chosen object of x . The Green's ratios for birth and death (namely, R_B and R_D ,

respectively) are.

$$R_B = \frac{p_D}{p_B} \frac{f_p(x'|I_g)}{f_p(x|I_g)} \frac{1}{n(x) + 1} \quad R_D = \frac{p_D}{p_B} \frac{f_p(x'|I_g)}{f_p(x|I_g)} n(x) \quad (11)$$

where $n(x)$ is the number of objects in the current configuration x and x' is the candidate configuration. For the selected non-jumping kernels (i.e., translation, dilation, and rotation), the suitable Green's ratio is given by the usual Metropolis-Hastings ratio

$$R(x, x') = \frac{f_p(x'|I_g)}{f_p(x|I_g)}. \quad (12)$$

3. EXPERIMENTAL RESULTS

Experiments were carried out using Mars data, collected during the 2001 Mars Odyssey mission, by the THERMAL EMISSION IMAGING SYSTEM (THEMIS), an instrument on board the Mars Odyssey spacecraft. Such an instrument combines a 5-band visual imaging system with a 10-band infrared imaging system [32]. Both 7 visible and 7 infrared THEMIS images, with a resolution of 18 meters and 100 meters per pixel, respectively, were used to test the proposed approach. In particular, the visible data set was chosen in the area with center longitude $lon = 352.86$ and center latitude $lat = -1.09$; the infrared data set was chosen within an area with $lon = 175.36$ and $lat = -14.68$.

Few parameters of the proposed method had to be assigned, concerning both the MPP state space S and the MCMC sampler. Let recall that $S = P \times K$, where $P = [0, M] \times [0, N]$ corresponds to the size of the data (I_g). The resolution r varies for the two different types of images used, hence the total area A of interest is $A = M \cdot N \cdot r^2$ [m²]. The parameters of K (i.e., a_m , a_M , b_m , and b_M) depend on the size of the objects that need to be detected. In this study, the minimum size for both semi-axes was fixed to 3 pixels (i.e., $a_m = b_m = 3$) and the maximum size to 100 pixels (i.e., $a_M = b_M = 100$). The eccentricity e

of each object, defined as

$$e = \sqrt{1 - \left(\frac{\min(a, b)}{\max(a, b)} \right)^2}, \quad (13)$$

was constrained to $e \in [0, 0.6]$ (i.e., $\min(a, b) \geq 0.8 \cdot \max(a, b)$), being craters of bigger e unlikely.

Sampler probabilities needed to be assigned as well. In particular, the global parameters that correspond to the probability of choosing the proposition kernel m were fixed to $p_m = 0.25$, where $m \in \{\text{Translation, Rotation, Scaling, Birth\&Death}\}$. The probabilities p_B and p_D regulating the birth and death kernel, were fixed to $p_B = p_D = 0.5$.

For comparison purposes, a method for ellipse detection based on a Generalized Hough Transform (GHT) [7] has been implemented and tested on our data set. With this method, for every pair of pixels that were detected as edge points in the Canny gradient and exhibit opposite gradient directions, an accumulator, corresponding to the median point between them in the image plane, is incremented by a unit value. The maxima of the accumulator are taken as centers of ellipses. Then, the three parameters describing the ellipse centered in each detected maximum are computed and a 3D accumulator is used to estimate the two semi-axes and the direction angle of the ellipse from all the pairs of points that contribute to the accumulator in the considered center. The results obtained by the proposed approach and by GHT were compared. This particular approach was chosen for comparison, being a standard technique for the detection of round and elliptical objects, commonly used for crater detection [12], [10], [11], [33].

Reference data were generated by manually analyzing each image of the data set and identifying all the craters that are present. Only objects completely included within the images were considered (i.e., objects cut by the borders of the image were discarded). A quantitative assessment of the obtained results by the proposed method was performed using these reference data. This was accomplished by comparing the obtained results with the labeled features in the correspondent reference map. The Detection percentage

Table 1. Average numerical performance of both the proposed approach (MPP) and a standard method (GHT) as measured by Detection percentage (D), Branching factor (B) and Quality percentage (Q).

| Data | Method | D | B | Q | Method | D | B | Q |
|---------|--------|-----|------|-----|--------|-----|------|-----|
| VIS | GHT | 73% | 0.24 | 62% | MPP | 82% | 0.22 | 71% |
| IR | GHT | 78% | 0.14 | 70% | MPP | 89% | 0.13 | 79% |
| Average | GHT | 75% | 0.20 | 65% | MPP | 85% | 0.18 | 74% |

D , the Branching factor B , and the Quality percentage Q were computed as follows:

$$D = \frac{100 \cdot TP}{TP + FN}; \quad B = \frac{FP}{TP}; \quad Q = \frac{100 \cdot TP}{TP + FP + FN} \quad (14)$$

where True Positive (TP) is the number of detected features that correspond to labeled objects in the reference map, False Positive (FP) is the number of features detected by the proposed approach, which do not correspond to any object in the reference map, and False Negative (FN) is the number of objects in the reference map that have not been detected by the proposed approach. The global values of D , B , and Q obtained by the proposed approach (MPP) and the standard method used for comparison (GHT) both for VIS and IR data are shown in Table 1. The global values of D for VIS data and IR data obtained by the proposed approach were about 82% and 89%, respectively. These high values indicate a good detection rate (because of the high number of TP). B was about 0.22 for VIS and 0.13 for IR, which indicate a small amount of false detections with respect to the true detections in both cases, thanks to the small number of FP . The results obtained by applying the proposed approach are more accurate when compared to the performance of the implemented standard technique based on the GHT. In particular, the average value of the detection rate D improved from 75% for the GHT to 85% for the MPP. This is explained by the increase in true detections with respect to the reference map. Similarly, the quality percentage Q . A relatively smaller improvement in the branching factor B is due to the fact that the number of FP was

already small when applying GHT.

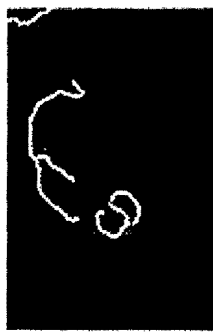
Moreover, the detection performance of the proposed approach in terms of D , B , and Q compares also favorably with most of the results previously published for automatic crater detection methods [13, 16, 34, 35]. Ideally, the performance of the proposed approach should be compared with the results obtained by the previously published methods when applied to the same data. Unfortunately, the performance of each published approach has been assessed on different sites and distinct types of data (e.g., panchromatic images, topographic data). The most direct performance comparison can be made with the method proposed by Barata *et al.* in [34]. That approach was tested on images acquired by the Mars Orbiter Camera (MOC). The method in [34] identified 546 craters, with $TP = 171$, $FN = 93$, and $FP = 282$. Hence, the resulting assessment factors were about $D = 65\%$, $B = 1.65$, and $Q = 31\%$. Bandeira *et al.* [13] proposed an unsupervised approach for crater detection from MOC data based on template matching. The average performances of that approach were about $D = 86\%$ and $Q = 84\%$. However, they tested their algorithm on images having resolution of 200-300m/pixel. The high performances obtained in [13] may be attributed to the fact that large craters in the sites of analysis have a very regular shape and are relatively easy to identify by template matching. The performance of that approach for the detection of small and irregular craters is unknown. Bue and Stepinski [35] proposed a supervised approach for crater detection from topographic data. The average performances of that approach were about $D = 74\%$, $B = 0.29$, and $Q = 61\%$. The evaluation factors increased to $D = 92\%$, $B = 0.29$, and $Q = 73\%$ if degraded craters, which the method was not able of detecting, were excluded. That approach is not fully comparable with the proposed method, being supervised. Urbach and Stepinski [16] proposed a supervised approach for crater detection from panchromatic images. The performance factors of their method were about $D = 68\%$, $B = 0.29$, and $Q = 57\%$, when detecting craters of diameter greater than 200m, and lower when taking into account also craters of smaller dimensions. However, a full comparison with our approach is again

not possible. In general, the results obtained by the proposed approach are comparable to, and in some cases better than results obtained by methods reported in the literature in terms of the assessment factors. Unfortunately, a full comparison is not possible, because the methods were applied to different data.

Visual results of the feature extraction are shown for the first band of a visible image (Fig. 3(a)). The image is first preprocessed, in order to reduce the noise. In particular, Gaussian filtering and median filtering operations are applied in a cascade [36] in order to reduce the noise and preserve the edges at the same time. The Canny edge detector is applied to the smoothed image and the binary gradient I_g is shown in Fig. 3-b. The estimated optimum configuration of the MPP x^* , which identifies the feature contours, is shown in Fig. 3-c. The optimum configuration x^* is represented in red, transparently superimposed to the original image. By a visual inspection, it is possible to appreciate the accuracy of the detection, even when many false alarms are present in the binary image gradient I_g . Also the reconstruction of the feature shape is very accurate.



(a) Original image



(b) Image edges



(c) Crater contours

Fig. 3. Experimental results obtained by applying the proposed method to the first band of a visible image. (a) Original image, (b) Canny gradient, and (c) detected crater contours in red, transparently superimposed to the original image.

Then, visual results obtained by applying the proposed approach to the eighth band of an infrared image (Figure 4-a) are presented. In particular, the Canny gradient I_g is shown in Fig. 4-b and the estimated x^* is shown in Figure 4-c, transparently superimposed to the original image. The contours of the represented crater appear non-continuous, in the binary image gradient I_g , due to the uneven quality of the image. Anyway, the feature is correctly detected and its shape reconstructed.

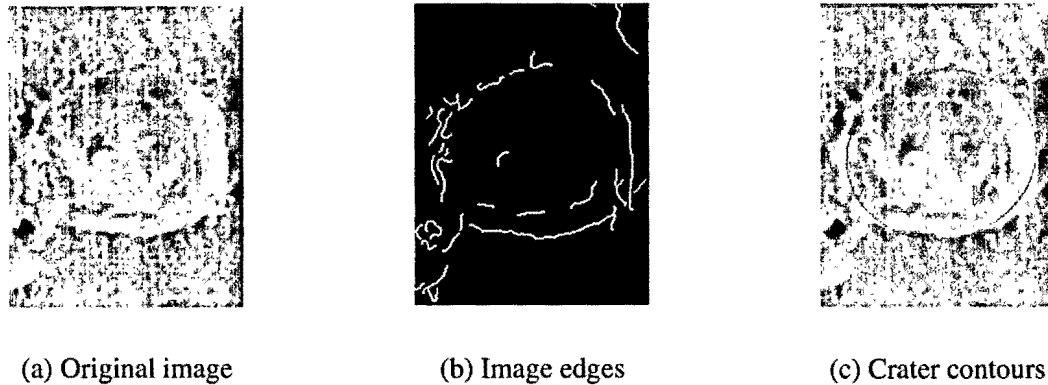


Fig. 4. Experimental results obtained by applying the proposed method to the eighth band of an infrared image. (a) Original image, (b) Canny gradient, and (c) detected crater contours in red, transparently superimposed to the original image.

A visual analysis of the detection results obtained with other planetary images (see Fig. 5) confirms that the proposed method is able to correctly identify the location and shape of the imaged craters, even though the input edge map detected only part of the crater borders, included many spurious contours unrelated with the craters, and was severely affected by the shadows in the crater area.

4. CONCLUSIONS

In this paper, a novel approach has been proposed for automatic detection of features that characterize planetary surfaces. The identification is achieved by using a method based on a Marked Point Process

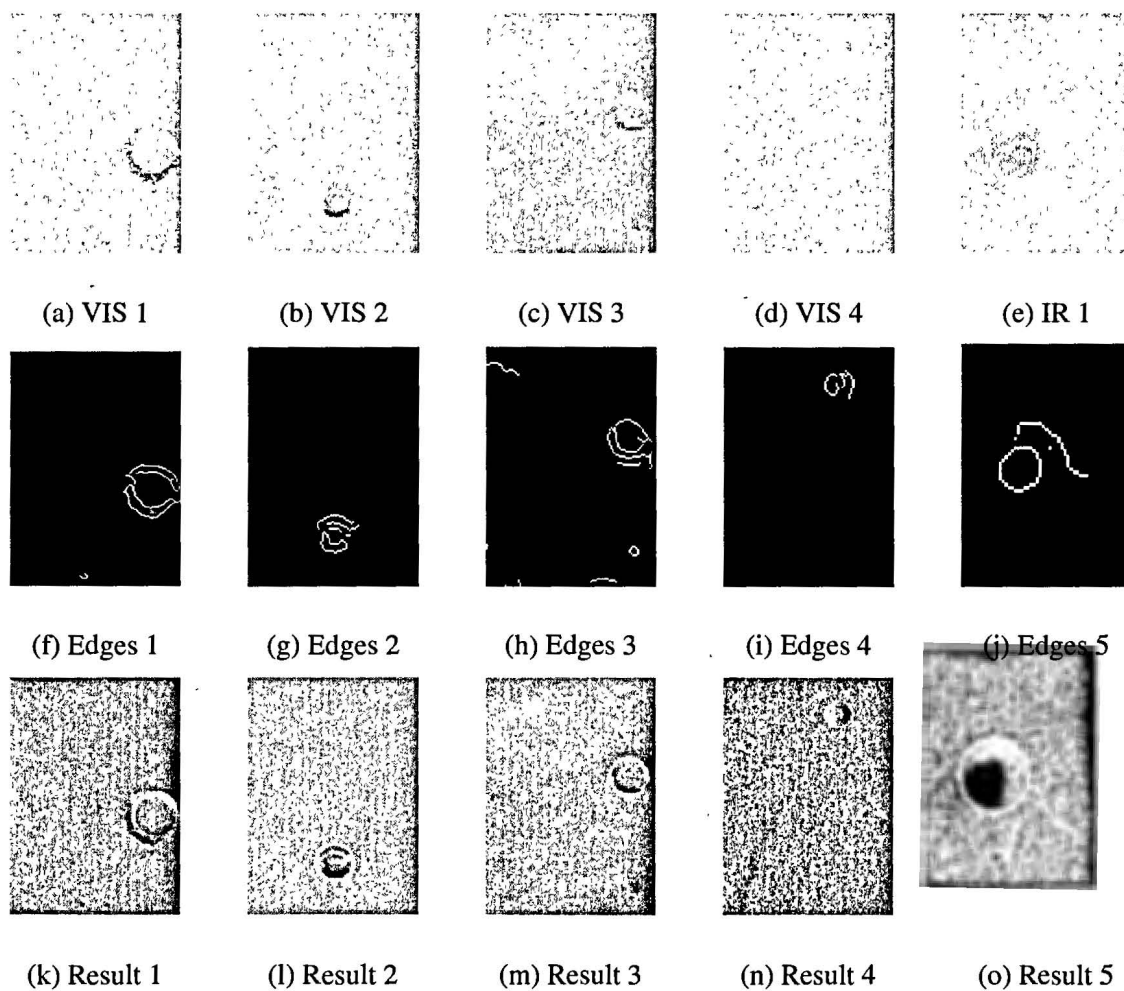


Fig. 5. Examples of experimental results obtained by the proposed method. (a), (b), (c), (d), (e) Original data, (f), (g), (h), (i), (j) respective edge maps, and (k), (l), (m), (n), (o) detected crater contours in red.

(MPP), coupled with a Markov chain and a simulated annealing scheme.

Mars infrared and visible multiband images, captured by THEMIS during the Mars Odyssey Mission, were used. Before the algorithm could be used to estimate the MPP optimum configuration, the images had to go through a preprocessing stage, aimed at obtaining contour map of the analyzed image. The likelihood between the extracted map and the current configuration was measured and maximized, in order to identify the optimum configuration.

The MPP approach, which was developed in the context of computer vision and previously used in many different applications (e.g., tree crown identification, road network detection, building extraction), has proven to be effective when applied to planetary images here. For such data, the features to be extracted are not as well contrasted nor defined as for Earth data. Nevertheless, we showed here that their identification can be accurately achieved. The accuracy of the detection has been assessed by a comparison to a manually generated reference map. The method outperformed a standard method for crater detection based on a generalized Hough transform, in terms of several indices based on true positives, false negatives, and false positives. Moreover, the obtained results compared favorably to most previously proposed approaches, when performances reported in the literature were considered for the same indices. Finally, a visual inspection of the detection results confirmed that the proposed method was also able to correctly identify the location and shape of the detected craters.

The proposed approach can be adopted as the first important step in several applications dealing with all the various data that are being collected during the current and future planetary missions. Among them selecting safe landing sites, identifying planetary resources, and preparing for subsequent planetary exploration by humans and robots. In our future work we will investigate the use of an illumination correction to improve the reliability of the detection for all craters, when shadows are present. The proposed approach will also be applied to the registration of multisensor and multitemporal images, by performing feature

matching.

Acknowledgment

This research was supported in part by the Research of Fund of the University of Iceland.

Appendix

In the following appendices details about Marked Point Processes (MPPs) and Reversible Jump Monte Carlo Markov Chain algorithm (RJMCMC) are given.

A. Marked Point Process

Given a bounded subset P of \mathbb{R}^2 , a point process X is a measurable mapping from a probability space (Ω, \mathcal{A}, P) to configurations of points on P , i.e., a random variable whose realizations are random configurations x of points:

$$x = \{x_1, \dots, x_n\}, \quad (15)$$

where x_i represents the position of the i -th point in the image plane (i.e., $i = 1, 2, \dots, n$).

These configurations belong to a measure space $(\Psi, \mathcal{B}(\Psi), \mu)$, where Ψ is the collection of all finite subsets of P , $\mathcal{B}(\cdot)$ is a σ -algebra over Ψ , and μ is a measure of the configuration space.

An MPP is a point process defined by a density function with respect to the Poisson measure (see below) [37], [38]. A configuration of an MPP consists of a set of marked points. A set of random parameters (called mark) is associated with each point. In image analysis, these parameters define some geometric property of an underlying object attached to that point, so that each realization of an MPP represents a

model for the possible spatial distribution of several objects in the image plane. The marks are parameters that fully describe the related geometric object. In particular, ellipses are described by three parameters, i.e., their major and minor axes and their orientation.

Hence, let X be an MPP defined in $S = P \times K$, a bounded set of \mathbb{R}^d , where P has the same meaning as above and K is the space of the marks describing the object geometry. The MPP X is still a measurable mapping from a probability space (Ω, A, \mathbb{P}) to configurations of points in S .

The probability distribution of an MPP is uniformly continuous [26] with respect to the Poisson measure μ of intensity λ on S . We recall that, given a Polish space E (i.e., a space homeomorphic to a complete metric space that has a countable dense subset) with a σ -finite measure λ on E , we call a random measure μ on E a Poisson measure with intensity λ if it satisfies the following conditions: For every Borel subset B of E with $\lambda(B) < +\infty$, $\mu(B)$ has a Poisson distribution with parameter $\lambda(B)$, and if B_1, \dots, B_n are disjoint Borel sets, the variables $\mu(B_1), \dots, \mu(B_n)$ are independent [39].

Operatively, it can be proven that X can be characterized by a density $f(\cdot)$ with respect to μ . $f(\cdot)$ is actually an unnormalized density and can be defined with respect to this dominating reference measure as:

$$P_X(D) = P\{X \in D\} = \frac{1}{Z} \int_D f d\mu, \quad (16)$$

for any Borel subset D of E , where Z is a normalizing constant.

B. Reversible Jump Markov Chain Monte-Carlo

In [31], Green proposed an algorithm to build a Markov Chain X , which ergodically converges to the probability distribution $P_X(\cdot)$. This algorithm can be summarized in the four steps that are listed below.

Given the probability space (Ω, A, \mathbb{P}) , let π be an unnormalized measure on Ω . The Reversible Jump Monte Carlo Markov Chain algorithm (RJMCMC) consists of defining a proposition kernel $Q(x, E)$,

where $x \in \Omega$ and E belongs to the σ -algebra A . The algorithm is based on the assumption that there exists a symmetrical measure ξ on $\Omega \times \Omega$ dominating the product measure $\pi(x)Q(x, E)$, i.e., there exists a measurable function h (namely, the Radon-Nikodym derivative), such that:

$$\int_{D \times E} h d\xi = \int_D Q(x, E) d\pi(x) \quad \forall D, E \in A. \quad (17)$$

The algorithm is the following:

- 1: Initialize x .
- 2: Generate the candidate configuration x' by choosing a proposition kernel $Q_m(x, \cdot)$ with probability p_m .
- 3: Compute the Green's ratio $R = \frac{h_m(x', x)}{h_m(x, x')}$, where h_m is the Radon-Nikodym derivative corresponding to the proposition kernel Q_m .
- 4: Accept the new state x' with probability $\alpha = \min(1, R)$.

When the RJMCMC is integrated within a simulated annealing framework, the Green's ratio R is replaced by $R^{1/T(k)}$, where $T(k)$ is the annealing schedule at the iteration k .

The efficiency of the algorithm highly depends on the variety of the proposition kernels Q . For the model considered in this article, the proposition kernel is defined as a combination of kernels defining birth, death, and the different non-jumping moves (translation, rotation, scaling of each single object in the configuration). Birth and death are jumping perturbations, i.e, they vary the number of objects in the configuration. If birth is chosen, a new marked point is randomly generated and added to the configuration, while if death is chosen a randomly selected point in the configuration is removed. Non-jumping moves are transformations that do not change the number of objects in the configuration. In particular, a marked point is randomly selected and is replaced by a "perturbed" version of it. Perturbations can be translation, rotation, and axis dilation.

5. REFERENCES

- [1] G. Salamuniccar and S. Loncaric, "Method for crater detection from martian digital topography data using gradient value/orientation, morphometry, vote analysis, slip tuning, and calibration," *IEEE Trans. Geosci. Remote Sens.*, vol. 48, pp. 2317–2329, 2010.
- [2] A. Flores-Mendez, *Crater Marking and Classification using Computer Vision*, vol. 2905, Springer-Verlag, New York, 2003.
- [3] T. Vinogradova, M. Burl, and E. Mjolsness, "Training of a crater detection algorithm for mars crater imagery," in *IEEE Aerospace Conference Proceedings*, 2002, vol. 7, pp. 3201–3211.
- [4] P. G. Wetzler, B. Enke, W. J. Merline, C. R. Chapman, and M. C. Burl, "Learning to detect small impact craters," in *IEEE Workshops on Applications of Computer Vision*, 2005, vol. 1, pp. 178–184.
- [5] R. Martins, P. Pina, J. S. Marques, and M. Silveira, "Crater detection by a boosting approach," *IEEE Geosci. Remote Sens. Lett.*, vol. 6, pp. 127–131, 2009.
- [6] P. Viola and M. Jones, "Robust real-time face detection," *Int. Journal of Computer Vision*, vol. 57, pp. 137–154, 2004.
- [7] S. Tsuji and F. Matsumoto, "Detection of ellipses by a modified Hough transformation," *IEEE Trans. on Computers*, vol. 27, 1978.
- [8] A. M. Cross, "Detection of circular geological features using the Hough transform," *International Journal of Remote Sensing*, vol. 9, pp. 1519–1528, 1988.
- [9] Y. Cheng, A. E. Johnson, L. H. Matthies, and C. F. Olson, "Optical landmark detection for spacecraft navigation," in *13th Annual AAS/AIAA Space Flight Mech Meeting*, Feb. 2002.

- [10] R. Honda, Y. Iijima, and O. Konishi, "Mining of topographic feature from heterogeneous imagery and its application to lunar craters," in *Progress in Discovery Science*, Setsuo Arikawa and Ayumi Shinohara, Eds., vol. 2281 of *Lecture Notes in Computer Science*, pp. 27–44. Springer Berlin / Heidelberg, 2002.
- [11] B. Leroy, G. Medioni, A. E. Johnson, and L. H. Matthies, "Crater detection for autonomous landing on asteroids," *Image and Vision Computing*, vol. 19, pp. 787–792, 2001.
- [12] G. Michael, "Coordinate registration by automated crater recognition," *Planetary Space Sci.*, vol. 51, pp. 563–568, 2003.
- [13] L. Bandeira, J. Saraiva, and P. Pina, "Impact crater recognition on mars based on a probability volume created by template matching," *IEEE Trans. Geosci. Remote Sens.*, vol. 45, pp. 4008–4015, 2007.
- [14] J. R. Kim and J.-P. Muller, "Impact crater detection on optical images and DEM," in *ISPRS Extraterrestrial Mapping Workshop "Advances in Planetary Mapping"*, Houston, TX, 2003.
- [15] J. R. Kim, J.-P. Muller, S. van Gasselt, J. G. Morley, and G. Neukum, "Automated crater detection, a new tool for mars cartography and chronology," *Photogrammetric Engineering and Remote Sensing*, vol. 71, no. 10, pp. 1205–1217, 2005.
- [16] E. R. Urbach and T. F. Stepinski, "Automatic detection of sub-km craters in high resolution planetary images," *Planetary and Space Science*, vol. 57, pp. 880–887, 2009.
- [17] M. van Lieshout, *Marked Point Processes and their Applications*, Imperial College Press, London, 2000.

- [18] G. Troglio, J. A. Benediktsson, G. Moser, and S. B. Serpico, "Crater detection based on marked point processes," in *IEEE International Geoscience and Remote Sensing Symposium*, 2010.
- [19] X. Descombes and J. Zerubia, "Marked point processes in image analysis," *IEEE Signal Processing Magazine*, vol. 19, no. 5, pp. 77–84, 2002.
- [20] F. Cerdas, X. Descombes, and J. Zerubia, "Urban scene rendering using object description," in *IEEE International Geoscience and Remote Sensing Symposium*, 2003, vol. 1, pp. 62–64.
- [21] M. Ortner, X. Descombes, and J. Zerubia, "A marked point process of rectangles and segments for automatic analysis of digital elevation models," *IEEE Trans. Pattern Analysis and Machine Intelligence*, , no. 1, pp. 105–119, 2008.
- [22] M. Quartulli and M. Datcu, "Stochastic geometrical modeling for built-up area understanding from a single sar intensity image with meter resolution," *IEEE Transactions on Geoscience and Remote Sensing*, vol. 42, no. 9, pp. 1996–2003, 2004.
- [23] G. Perrin, X. Descombes, and J. Zerubia, "Tree crown extraction using marked point processes," in *EUSIPCO Conf.*, Vienna, Austria, 2004.
- [24] J. Canny, "A computational approach to edge detection," *IEEE Trans. Pattern Anal. Mach. Intell.*, vol. 10, no. 6, 1986.
- [25] G. Perrin, X. Descombes, and J. Zerubia, "A marked point process model for tree crown extraction in plantations," in *IEEE ICIP*, 2005, pp. 661–664.
- [26] W. Rudin, *Principles of Mathematical Analysis*, 2nd edition, McGraw-Hill, New York, 1976.

- [27] G.K. Matsopoulos, N.A. Mouravliansky, K.K. Delibasis, and K.S. Nikita, "Automatic retinal image registration scheme using global optimization techniques," *IEEE Trans. on Information Technology in Biomedicine*, vol. 3, no. 1, pp. 47–60, 1999.
- [28] C. Geyer and J. Moller, "Likelihood inference for spatial point processes," *Stochastic Geometry, Likelihood and Computation*, 1998.
- [29] C. Robert and G. Casella, *Monte Carlo statistical methods*, Springer-Verlag, New York, 1999.
- [30] G. Perrin, X. Descombes, and J. Zerubia, "Adaptive simulated annealing for energy minimization problem in a marked point process application," in *EMMCVPR Conference*, Saint Augustine, FL, 2005.
- [31] P.J. Green, "Reversible jump Markov chain monte carlo computation and Bayesian model determination," *Biometrika*, vol. 82, pp. 711–732, 1995.
- [32] P. Christensen, B. M. Jakosky, H. H. Kieffer, M. C. Malin, H. Y. Mcsween, K. Nealson, G. L. Mehalland S. H. Silverman, S. Ferry, M. Caplinger, and M. Ravine, "The thermal emission imaging system (THEMIS) for the mars 2001 odyssey mission," *Space Science Reviews*, vol. 100, pp. 85–130, 2004.
- [33] G. Troglio, J. Le Moigne, J. A. Benediktsson, G. Moser, and S. B. Serpico, "Automatic extraction of planetary image features," in *IEEE International Conference on Space Mission Challenges for Information Technology*, 2009, pp. 211–215.
- [34] T. Barata, E. I. Alves, J. Saraiva, and P. Pina, *Automatic Recognition of Impact Craters on the Surface of Mars*, vol. 3212, Springer-Verlag, Berlin, Germany, 2004.

- [35] B. D. Bue and T. F. Stepinski, "Machine detection of martian impact craters from digital topography data," *IEEE Trans. Geosci. Remote Sens.*, vol. 45, pp. 265–274, 2007.
- [36] L. G. Shapiro and G. C Stockman, *Computer Vision*, Prentence Hall, 2001.
- [37] D. Stoyan, W.S. Kendall, and J. Mecke, *Stochastic Geometry and its Applications*, Wiley, New York, 1987.
- [38] B. D. Ripley, "Modelling spatial patterns," *Royal Statistical Institute*, vol. 39, pp. 172–212, 1997.
- [39] J. Bertoin, *Levi processes*, Cambridge University Press, Cambridge, 1998.